Journal of Physics B: Atomic, Molecular and Optical Physics

PAPER

Ionization cross sections of the L subshells of Au by 50 to 100 keV electron impact

To cite this article: S F Barros *et al* 2015 *J. Phys. B: At. Mol. Opt. Phys.* **48** 175201

IOP Publishing Journal of Physics B: Atomic, Molecular and Optical Physics

J. Phys. B: At. Mol. Opt. Phys. **48** (2015) 175201 (12pp) doi:10.1088/0953-4075/48/17/175201

Ionization cross sections of the L subshells of Au by 50 to 100 keV electron impact

S F Barros[1], V R Vanin[1], N L Maidana[1] and J M Fernández-Varea[1,2]

[1] Instituto de Física, Universidade de São Paulo. Rua do Matão, Travessa R 187, Cidade Universitária, CEP: 05508-900 São Paulo, SP, Brazil
[2] Facultat de Física (ECM and ICC), Universitat de Barcelona. Diagonal 645, E-08028 Barcelona, Spain

E-mail: suelenb@if.usp.br

Received 23 January 2015, revised 22 April 2015
Accepted for publication 5 June 2015
Published 17 July 2015

Abstract

We have measured the Lα, Lβ, Lγ_1, Lγ_2, Lγ_3, Lℓ and Lη x-ray production cross sections of Au by 50–100 keV electron impact. From this experimental information we derived the L_1, L_2 and L_3 subshell ionization cross sections with a novel analysis procedure that is based on an overdetermined system of equations and achieve the estimates by the least-squares method. The uncertainties in the atomic relaxation parameters needed to transform the x-ray intensities to ionization cross sections impose a lower limit to the relative standard deviations of the L subshell ionization cross sections, which is found to be 5–10% depending on the selected set of relaxation parameters. Our experimental results are in reasonable accord with most of the measurements carried out by other authors, and they agree with the predictions of the semi-relativistic distorted-wave Born approximation.

Keywords: atomic L subshells, electron-impact ionization, distorted-wave Born approximation

(Some figures may appear in colour only in the online journal)

1. Introduction

Measurements of atomic inner-shell ionization cross sections by electron impact have been the subject of continuing research for at least 80 years and continues even now [1]. The vast majority of experimental data refers to the K shell. Measurements for the L shell are more limited, and they are even more scarce for the M shell. Absolute L (sub)shell ionization cross sections have only been published for sixteen elements [1]. Moreover, the available experimental values are affected by large uncertainties, and data from different authors show significant discrepancies [1]. This situation can be ascribed to the difficulty in determining the ionization cross section for subshells outer than the K shell. In the case of the K shell, the intensity of the characteristic x-rays is just a function of the corresponding ionization cross section, while for the other shells it depends on the ionization cross sections of all the respective subshells due to the intra-shell displacement of vacancies produced by Coster–Kronig transitions. The same difficulties are also present in measurements of ionization cross sections by proton impact [2]. Therefore, since the experimental data pertain to x-ray production cross section and not ionization cross section, determining the latter requires the knowledge of atomic relaxation parameters, namely Coster–Kronig coefficients, vacancy-transfer probabilities from one shell to another, fluorescence yields and rates of x-ray emission which, however, are generally poorly known. The evaluation of the cross section uncertainties poses an additional challenge because the experimental uncertainties of the relaxation parameters (about 25 in L-shell ionization) must be propagated to each subshell ionization cross section. Owing to these complications, a common practice in the literature on L and M subshells is to report the x-ray production cross sections rather than the L or M (sub) shell ionization cross sections [1].

In this paper we describe new measurements of Au ($Z = 79$) Lα, Lβ, Lγ, Lℓ and Lη x-ray production cross sections by the impact of electrons with kinetic energies from 50 to 100 keV. To our knowledge, the Lℓ and Lη x-ray production cross sections of Au are reported here for the first time in this energy interval. We also propose a novel methodology to derive the L_1, L_2 and L_3 subshell ionization cross sections applying the least-squares method with a design matrix based on the relations between subshell ionization and

x-ray production cross sections. Besides, the uncertainties of the atomic relaxation parameters were propagated to the uncertainties of the estimated ionization cross sections. Our results are compared with the distorted-wave Born aproximation (DWBA) [3, 4] and with experimental data from the literature. In this energy interval there are just a few measurements of the L_1, L_2 and L_3 subshell ionization cross sections [5–11]. Unfortunately, the values reported in these references are not consistent and, in some cases, they depart considerably from the calculations based on the DWBA. Furthermore, none of these works accounted for the contribution of the atomic relaxation parameters in the cross section uncertainty budget. Our experimental cross sections span from 50 to 100 keV and are thus complementary to the recent measurements by Rahangdale *et al* [11] which extend from the ionization threshold to 40 keV.

2. Experiment

A thin target was irradiated in the São Paulo Microtron electron accelerator (Instituto de Física, Universidade de São Paulo, Brazil) in the beam line and vacuum chamber already described in [12]. The characteristic x-rays emitted by the ionized atoms and the bremsstrahlung photons were observed with a planar HPGe detector.

2.1. Sample and irradiation chamber

A thin film of Au deposited on a thin C backing was prepared using the physical vapour deposition technique. The target substrate was obtained by evaporation of C onto a glass holder, and had a thickness of 10(5) μg cm^{-2}. It was detached from the glass and subsequently attached to the sample frame, a rectangle with 30 mm and 15 mm sides, 0.7 mm thick and a central hole 10 mm in diameter, made of C fiber to minimize the production of photons by electrons in the beam halo or scattered by the target, that yield undesired photoionization events. This framed backing was placed in an evaporator under vacuum, over a circular mask 8 mm in diameter, centered in the frame hole, to deposit a uniform film of Au by physical vapour deposition; this reduces the total amount of Au that could be hit by any background photon in the irradiation chamber. The mass thickness of Au was determined by fitting the tip of bremsstrahlung spectra with the procedure outlined in [12, 13], and the estimated value was 8.0(10) μg cm^{-2}. As a consequence, the x-ray production and ionization cross sections presented in this work depend on the theoretical bremsstrahlung differential cross section, and its uncertainty (around 10%) [14–16] is the most important component in the quoted uncertainty of the mass thickness.

An Al holder placed the target in the center of the irradiation chamber perpendicularly to the incident electron beam. A pneumatic arm drove this holder, and three positions were available to the experimentalist: beam on target, beam on view-screen and free passage to the Faraday cup. The choice of materials for the frame and sample holder aimed to minimize the background photon flux.

Not all the electrons of the beam that impinge on the sample arrive to the Faraday cup because they may scatter elastically while passing through the sample. In order to estimate the associated current loss, we made a sequence of ten alternate measurements of the current reaching the Faraday cup with and without the sample at the irradiation position. We determined the fraction of charge collected by the Faraday cup from the mean values of the ratios between two successive runs. In fact, a similar procedure was employed by Rahangdale *et al* [11] in their very recent work. Since the elastic scattering of the electrons in the target is energy dependent, we measured in each energy run the charge collected by the Faraday cup and the collection factor, and evaluated the number of electrons incident on the target from the ratio of these quantities.

2.2. Measurement of x-ray spectra

The experimental setup consisted in a Planar 1000 Series Hyper pure germanium Ortec low energy photon spectrometer (ORTEC Advanced Measurements Technology, Oak Ridge, USA), 5 cm^2 in area and 1 cm thick, with a 0.254 mm Be window. The detector was placed at 120° with respect to the beam direction and it observed the x-rays emitted by the sample through the Al spectroscopy window of the vacuum chamber. A cylindrical Cu collimator 70 mm in length and 10 mm aperture aligned with the axis of the Ge crystal suppressed most of the stray radiation.

The full-energy (FE) peak efficiency, $\epsilon_{\rm FE}(E)$, was determined from the γ-rays and characteristic x-rays emitted in the decay of ^{57}Co, ^{133}Ba, ^{137}Cs, ^{207}Bi and ^{241}Am radioactive sources. The ^{133}Ba and ^{207}Bi sources were produced and calibrated by Amersham, while the others were manufactured and calibrated absolutely at LMN-IPEN/CNEN-SP (Nuclear Metrology Laboratory, Institute of Nuclear Research and National Commission for Nuclear Energy, São Paulo). The calibration of the FE peak efficiency extends the procedure described in [17] to energies below the Ge K binding energy, $U_{\rm Ge\,K}$= 11.1 keV. In what follows we provide the details required for this extension and the formulas needed to evaluate the continuum part of the spectrum under the L x-ray peaks.

In a Ge detector there is a sudden change in the FE peak efficiency at $U_{\rm Ge\,K}$ due to the strong variation in photon attenuation. In addition, around and below this energy the important photon attenuation by the absorbers normally placed between the photon source and the detector cannot be ignored. In our setup, the irradiation chamber spectroscopy window is an Al foil, whose thickness was accurately known to be 50.0(5) μm. However, when the chamber is evacuated the Al foil gets slightly deformed assuming a spherical cap shape and its thickness reduces to 48.7(5) μm. Figure 1 shows the FE peak efficiency curve $\epsilon_{\rm FE}(E)$ along with the experimental data. Notice the sharp discontinuity at $U_{\rm Ge\,K}$ and the strong reduction below this energy. The only fitted parameter was the fraction of the solid angle defined by the detector, $\Omega/4\pi$. We point out that Seltzer's model [18], implemented as explained in [17], did not necessitate any change in order to

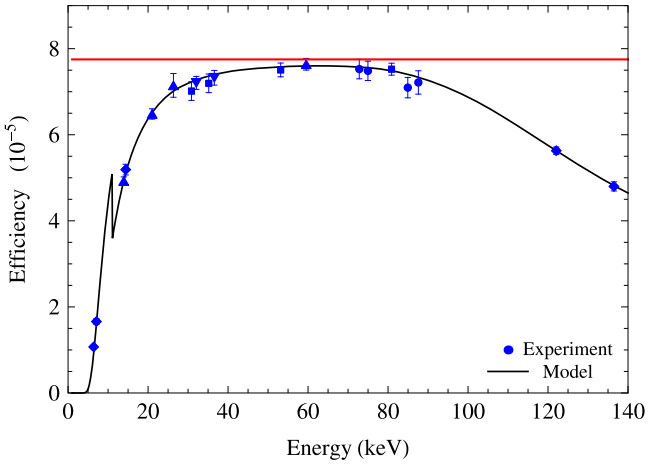

Figure 1. FE peak efficiency, $\epsilon_{\rm FE}(E)$, of the planar HPGe detector as a function of photon energy. The symbols are experimental values, and the error bars correspond to one standard deviation. The continuous curve is Seltzer's model [18] with the fraction of the solid angle covered by the detector fitted to the experimental values. The (red) horizontal line indicates the geometric detection efficiency, i.e. $\Omega/4\pi$.

be applied to this low-energy region; we only had to pay particular attention to the attenuation layers.

Since the Au L x-ray lines are located around $U_{\rm Ge\,K}$, the shape of the continuous part of the energy spectrum demands a model that is more complex than just a polynomial in the photon energy, except for the Lγ group, for which we adopted a second degree polynomial because this group falls in an energy region where the detection efficiency does not have any discontinuity and the energy interval is sufficiently narrow to neglect the variation in bremsstrahlung intensity. For the peaks corresponding to the Lα and Lβ groups, the continuous component of the spectrum is modelled as

$$y(E) = \Phi(E) + \mathcal{P}_{\rm K\alpha}(E) + \mathcal{P}_{\rm K\beta}(E) + a + b\big(E - E_0\big), \quad (1)$$

where $\Phi(E)$ describes the bremsstrahlung spectrum produced by the target, which plays a prominent role at low energies, $\mathcal{P}_{\rm K\alpha}(E) + \mathcal{P}_{\rm K\beta}(E)$ gives the counts from Ge K x-ray escape from the detector's active volume of photons with energy above that of the region of interest, and $a + b(E - E_0)$ accounts for the difference between the true target bremsstrahlung plus Ge K escape and the adopted models. The arbitrary constant (not a fit parameter) E_0 was set as the central point in the region of interest; this choice reduces strongly the statistical correlation between the fitted parameters a and b as compared to those that would be obtained with the value $E_0 = 0$ that is implicit in the form $a + bE$. Moreover, a is easier to interpret when E_0 is inside the fitting region.

Approximating the bremsstrahlung energy spectrum by ϕ_0/E', we define

$$\Phi(E) = \int_{E_{\rm min}}^{E_{\rm e}} \left(\phi_0/E'\right) \epsilon_{\rm FE}(E')\, R(E, E')\, {\rm d}E', \quad (2)$$

where ϕ_0 is an adjustable parameter, $E_{\rm e}$ is the electron beam energy and $E_{\rm min}$ is the smallest energy of interest. The detector response function, $R(E, E')$, consists of a Gaussian with dispersion $s(E) = \sqrt{s_{\rm el}^2 + W_{\rm Ge} F_{\rm Ge} E}$ plus a flat shelf with amplitude h [12]; $s_{\rm el}$ is the electronic noise associated with the pulse amplification process, whereas $W_{\rm Ge}$ and $F_{\rm Ge}$ are, respectively, the average energy expended in the formation of an electron-hole pair in Ge and the Fano factor [19]. Both the amplitude h of the complementary error function that models the flat shelf and the product $W_{\rm Ge} F_{\rm Ge}$ were previously calibrated; they are intrinsic properties of the detector and, unlike $s_{\rm el}$, do not depend on the count rate. We choose $E_{\rm min}$ smaller than the low-energy end of the fitting interval by about two peak widths to ensure a smooth behaviour of the convolution integral (2) in the region of interest. We took

$$\mathcal{P}_{\rm K\alpha}(E) = n\big(E + E_{\rm Ge\,K\alpha}\big)\, p_{\rm K\alpha}\big(E + E_{\rm Ge\,K\alpha}\big), \quad (3)$$

where $n(E')$ is the number of counts in the observed spectrum at energy E' and $p_{\rm K\alpha}(E')$ is the probability of Ge Kα x-ray escape through the detector front surface, see e.g. equation (12) in [18]; $E_{\rm GeK\alpha}$ is the average energy of the Kα doublet [20]. Similar expressions hold for $\mathcal{P}_{\rm K\beta}$ and $p_{\rm K\beta}$. Note that Ge K x-ray escape is by far the most important secondary detection effect at the energies of interest.

We employed a digital spectrometer, DSPEC from ORTEC, which integrates and differentiates numerically the preamplifier pulse digitized at a high rate (10 MHz). The pulse shaping parameters were selected to reduce pile-up while keeping an acceptable resolution: rise time of 4.0 μs and flattop width of 0.5 μs. The energy resolution (FWHM) was about 460 eV at the Fe Kα line (6.4 keV) of the ^{57}Co source. We used the MAESTRO software (ORTEC, Oak Ridge, USA) to control the acquisition of the x-ray spectra.

The irradiations were carried out at 51.07, 56.46, 61.07, 65.85, 70.45, 79.96, 89.88 and 100.43 keV with an uncertainty of 40 eV for all energies. These energies, as well as the respective uncertainties, were estimated by fitting the tip of the bremsstrahlung of each spectrum as described in [12]. For each electron energy, two spectra with 600 s live counting time were recorded. The dead time of the photon spectroscopy system was maintained below 5% in all runs. This condition was achieved varying the beam current between 100 and 550 nA, depending on the x-ray detection rate. A typical spectrum is depicted in figure 2.

3. Data Analysis

3.1. X-ray production cross sections

We assume that electrons penetrate the film of the studied element and follow a straight trajectory without losing energy, which is valid for thin films and electron beams with not too low energies. The experimental Lj x-ray production cross sections in the run with electrons of energy E are given by

$$\sigma_{{\rm L}j}^{\rm x}(E) = \frac{N_{{\rm L}j}}{N_{\rm e}\, \mathcal{N}d\, \epsilon_{\rm FE}\big(E_{{\rm L}j}\big)}, \quad (4)$$

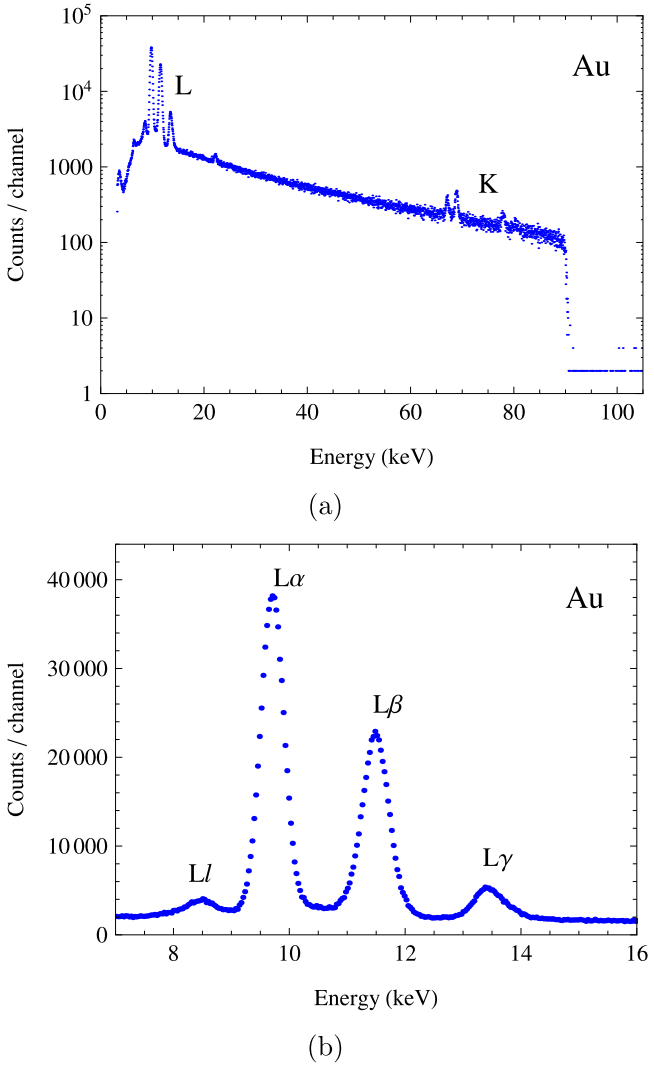

Figure 2. X-ray energy spectrum emitted by the Au sample in the run with 89.88(4) keV electrons. The dispersion in energy is 32 eV per channel. (a) Complete spectrum (log scale). (b) Region of the characteristic L x-rays.

where N_{Lj} is the area of the Lj peak (energy E_{Lj}), $\mathcal{N}$ is the number of Au atoms per unit volume, d is the Au film thickness and N_e is the number of incident electrons, which was estimated from the charge collected in the Faraday cup as described in section 2. The emission of characteristic L x-rays is regarded to be isotropic.

The parameters of the lines in the Lβ and Lγ groups were fitted separately, and those of the Lα doublet and the Lℓ and Lη lines were fitted simultaneously. The detector resolution in the region of interest did not allow the lines of the Lα and Lβ groups to unfold. However, it was possible to approximately separate the contributions of the Lγ_1, Lγ_2 and Lγ_3 lines of the Lγ multiplet. The x-ray peaks were fitted with a Gaussian shape because the resolution of the HPGe detector is insufficient to unveil the intrinsic Lorentzian shape of x-ray transitions, which would require the use of a Voigt function [21]. In each group, we left the position x_{ref} of a single line as a free parameter and held the position of the others fixed relative to this parameter based on the experimental x-ray energies from [20].

We fitted, by the least-squares method, the parameters of the function

$$\sum_{Lj} N_{Lj}\, G\Big(x_{Lj},\, s\big(E_{Lj}\big);\, x\Big) + y\big(\phi_0,\, s_{el},\, a,\, b;\, x\big), \qquad (5)$$

where x is the channel number, the sum extends to every line in the group of interest, and $G(x_{Lj}, s; x)$ is a Gaussian function with average x_{Lj} and standard deviation s. When all but one of the peak positions are fixed, expression (5) is linear in each parameter with the sole exceptions of the peak position x_{ref} of the line chosen as reference and the electronic noise contribution s_{el} to the dispersion s. Then, assigning values to these two parameters, the peak areas N_{Lj} and the coefficients ϕ_0, a and b of the continuum component can be determined by the least-squares method using a non-iterative procedure. This allows the search for the fitting parameters in a graphical way, looking for the values of x_{ref} and s_{el}^2 that minimize the two-dimensional merit function

$$\hat{Q}\Big(x_{ref},\, s_{el}^2\Big) = \Big(\mathbf{y}_{exp} - \hat{\mathbf{y}}\Big)^{T}\, \mathbb{V}_{exp}^{-1}\Big(\mathbf{y}_{exp} - \hat{\mathbf{y}}\Big), \qquad (6)$$

where $\mathbf{y}_{exp}$ is the column vector with the experimental spectrum, $\hat{\mathbf{y}}$ is the column vector with count values calculated for N_{Lj}, ϕ_0, a and b fitted by a *linear* least-squares procedure taking s_{el}^2 and x_{ref} as fixed constants, and $\mathbb{V}_{exp}$ is the variance matrix of the experimental data $\mathbf{y}_{exp}$. Hence, the hat in symbol $\hat{Q}$ means that N_{Lj}, ϕ_0, a and b give the minimum of Q for the given pair of parameters (x_{ref}, s_{el}^2). The contour lines of $\hat{Q}$ are drawn and the position of the minimum gives the estimates $\hat{x}_{ref}$ and $\hat{s}_{el}^2$; the amplitudes N_{Lj} calculated for $\hat{x}_{ref}$ and $\hat{s}_{el}^2$ are the least-squares estimates that we were seeking. Notice that the parameter h of the response function was evaluated from the prior calibration with radioactive sources along with the product $W_{Ge}F_{Ge}$, which was fitted to the FWHM of the peaks of the most intense transitions using the adopted formula for $s(E)$; these are intrinsic properties of the detector, and there is not enough statistics in this small energy region to fit them. All the calculations were performed with the Mathematica 9.0.1 program.

Figure 3 shows the continuum component of the spectrum under the Lℓ, Lα and Lβ peaks in the run with 65.85(4) keV electrons. The arrow indicates the energy $U_{Ge\,K}$ where the discontinuity of the detector efficiency is located. Contour curves of $\hat{Q}(x_{ref}, s_{el}^2)$ and fitted lines of the Lγ multiplet for the 89.88(4) keV electron beam are presented in figure 4. The reduced χ^2 for this fit was 1.03 with a probability of being exceeded equal to 41%. We determined the total number of counts of the group of lines in each multiplet by summing the counts in the region of interest and subtracting the continuous part, which was evaluated from the parameters fitted to the continuum component of the spectrum.

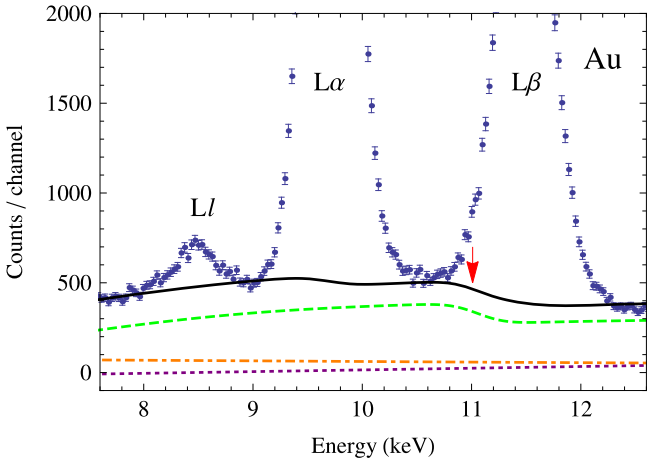

Figure 3. Lℓ, Lα and Lβ x-ray spectrum region in the run with 65.85(4) keV electrons. The dispersion in energy is 32 eV per channel. The continuum component of the spectrum, equation (1), is plotted as a (black) continuous curve. The (green) dashed curve is the contribution of bremsstrahlung produced by the target, $\Phi(E)$, and the (orange) dot-dashed curve pertains to the escape of Ge K x-rays, $\mathcal{P}_{K\alpha}(E) + \mathcal{P}_{K\beta}(E)$. The (violet) dotted curve indicates $a + b(E - E_0)$. The arrow marks the energy $U_{\mathrm{Ge\,K}}$.

3.2. L-subshell ionization cross sections

The x-ray production cross sections for the most intense peaks and lines in the L series are related to the L_i subshell ionization cross sections by means of the corresponding vacancy-production cross sections $\sigma^{\mathrm{h}}_{L_i}$ through the relations (see e.g. [1, 22])

$$\sigma^{\mathrm{x}}_{L\alpha} = \frac{\Gamma_{3\alpha}}{\Gamma_{3,\mathrm{tot}}}\,\omega_3\,\sigma^{\mathrm{h}}_{L_3}, \tag{7}$$

$$\sigma^{\mathrm{x}}_{L\beta} = \frac{\Gamma_{3\beta}}{\Gamma_{3,\mathrm{tot}}}\,\omega_3\,\sigma^{\mathrm{h}}_{L_3} + \frac{\Gamma_{2\beta}}{\Gamma_{2,\mathrm{tot}}}\,\omega_2\,\sigma^{\mathrm{h}}_{L_2} + \frac{\Gamma_{1\beta}}{\Gamma_{1,\mathrm{tot}}}\,\omega_1\,\sigma^{\mathrm{h}}_{L_1}, \tag{8}$$

$$\sigma^{\mathrm{x}}_{L\ell} = \frac{\Gamma_{L_3M_1}}{\Gamma_{3,\mathrm{tot}}}\,\omega_3\,\sigma^{\mathrm{h}}_{L_3}, \tag{9}$$

$$\sigma^{\mathrm{x}}_{L\eta} = \frac{\Gamma_{L_2M_1}}{\Gamma_{2,\mathrm{tot}}}\,\omega_2\,\sigma^{\mathrm{h}}_{L_2}, \tag{10}$$

$$\sigma^{\mathrm{x}}_{L\gamma_1} = \frac{\Gamma_{L_2N_4}}{\Gamma_{2,\mathrm{tot}}}\,\omega_2\,\sigma^{\mathrm{h}}_{L_2}, \tag{11}$$

$$\sigma^{\mathrm{x}}_{L\gamma_2} = \frac{\Gamma_{L_1N_2}}{\Gamma_{1,\mathrm{tot}}}\,\omega_1\,\sigma^{\mathrm{h}}_{L_1}, \tag{12}$$

$$\sigma^{\mathrm{x}}_{L\gamma_3} = \frac{\Gamma_{L_1N_3}}{\Gamma_{1,\mathrm{tot}}}\,\omega_1\,\sigma^{\mathrm{h}}_{L_1}, \tag{13}$$

where ω_i is the fluorescence yield of subshell L_i, $\Gamma_{i\alpha}$ and $\Gamma_{i\beta}$ are emission rates for transitions belonging to the Lα and Lβ groups, respectively, $\Gamma_{L_iM(N)_j}$ is the emission rate for the transition $L_iM(N)_j$, and $\Gamma_{i,\mathrm{tot}}$ is the sum of the emission rates for all possible transitions to the L_i subshell. In the Lα, Lβ and Lγ x-ray series we only included the most intense dipole-allowed transitions, see table I in [23]. For instance, Lγ_4 is a line of low intensity which requires high counting statistics to be resolved, and it was consequently not included. In the case of line Lγ_5, the fitted amplitudes were compatible with zero in all the spectra, therefore they were re-analysed removing Lγ_5 from the list of adjustable parameters.

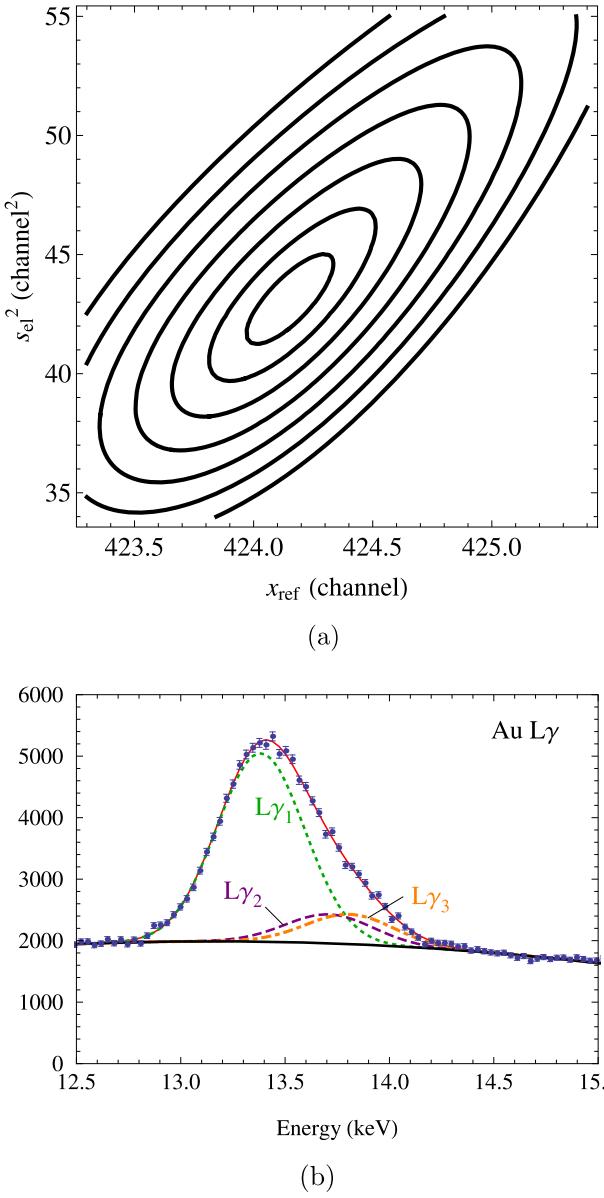

Figure 4. (a) Level curves of the merit function $\hat{Q}(x_{\mathrm{ref}}, s^2_{\mathrm{el}})=\chi^2+ n^2$, n=1...7 equation (6), and (b) fitted contributions of the Lγ_1, Lγ_2 and Lγ_3 lines to the Lγ multiplet, in the run with 89.88(4) keV electrons. x_{ref} is the centroid of the Lγ_1 line. The thick (black) curve under the Lγ peak represents the fitted continuum component of the energy spectrum.

The vacancy-production cross sections are in turn related to the K, L_1, L_2 and L_3 (sub)shell ionization cross sections σ_{K}, σ_{L_1}, σ_{L_2} and σ_{L_3} through the expressions (see e.g. [1, 22])

$$\sigma^{\mathrm{h}}_{L_1} = \sigma_{L_1} + \eta_{KL_1}\,\sigma_{\mathrm{K}}, \tag{14}$$

$$\sigma^{\mathrm{h}}_{L_2} = \sigma_{L_2} + f_{12}\,\sigma_{L_1} + \left(\eta_{KL_2} + f_{12}\,\eta_{KL_1}\right)\sigma_{\mathrm{K}}, \tag{15}$$

$$\sigma^{\mathrm{h}}_{\mathrm{L}_3} = \sigma_{\mathrm{L}_3} + f_{23}\,\sigma_{\mathrm{L}_2} + \left(f_{13} + f'_{13} + f_{12}f_{23}\right)\sigma_{\mathrm{L}_1} + \left(\eta_{\mathrm{KL}_3} + f_{23}\eta_{\mathrm{KL}_2} + \left(f_{13} + f'_{13} + f_{12}f_{23}\right)\eta_{\mathrm{KL}_1}\right)\sigma_{\mathrm{K}}, \tag{16}$$

where f_{ij} are the Coster–Kronig non-radiative transition probabilities, f'_{13} is the Coster–Kronig radiative transition probability and η_{KL_i} are the vacancy-transfer probabilities from the K shell to the L_i subshells. The contribution of intrashell radiative transitions from L_1 to L_2 have not been included in equations (15) and (16) owing to the extremely low value of the corresponding yield f'_{12}. Recall that the terms proportional to σ_{K} are non-zero only for energies above the Au K binding energy ($U_{\mathrm{Au\,K}}$= 80.7 keV [20]).

Many combinations of equations (7) to (13) have been used to determine the L_1, L_2 and L_3 subshell ionization cross sections. Cohen [24] reviewed various methodologies employed to extract ionization cross sections from x-ray production cross sections. Reusch *et al* [25] measured ionization cross sections resorting to a procedure that avoids the previous knowledge of the Lα, Lβ and Lγ x-ray production cross sections. However, this method needs the intensities of these multiplets and the L-shell ionization cross section, which is known for few elements and with low accuracy.

Our proposal consists in using the x-ray production cross sections of *all* the observed lines or groups to derive the ionization cross sections for the L_1, L_2 and L_3 subshells from the ensuing overdetermined system of equations by the least-squares method, and evaluate standard deviations that account for the uncertainties due to the atomic relaxation parameters besides those arising from the statistical uncertainties in our experiment. In this work, we chose expressions (7) to (13) with the x-ray production cross sections of the Lα and Lβ multiplets and the Lℓ, Lη, Lγ_1, Lγ_2 and Lγ_3 lines.

Expressions (7) to (13) can be cast in matrix form

$$\boldsymbol{\sigma}^{\mathrm{x}}_0 = \mathbb{X}\,\boldsymbol{\sigma}_0, \tag{17}$$

where $\boldsymbol{\sigma}^{\mathrm{x}}_0$ is the column vector with true values of the x-ray production cross sections, $\boldsymbol{\sigma}_0$ is the column vector with the true values for L subshell ionization cross sections and $\mathbb{X}$ is the rectangular design matrix, which is built from the selected atomic relaxation parameters. Our goal is to find an estimate $\hat{\boldsymbol{\sigma}}$ for the vector $\boldsymbol{\sigma}_0$, taking the experimental data $\boldsymbol{\sigma}^{\mathrm{x}}_{\mathrm{exp}}$ as estimates of $\boldsymbol{\sigma}^{\mathrm{x}}_0$. We seek $\hat{\boldsymbol{\sigma}}$ that minimizes

$$\Theta(\hat{\boldsymbol{\sigma}}) = \left(\boldsymbol{\sigma}^{\mathrm{x}}_{\mathrm{exp}} - \hat{\boldsymbol{\sigma}}^{\mathrm{x}}\right)^{\mathrm{T}} \mathbb{V}^{-1}_{\boldsymbol{\sigma}^{\mathrm{x}}_{\mathrm{exp}}} \left(\boldsymbol{\sigma}^{\mathrm{x}}_{\mathrm{exp}} - \hat{\boldsymbol{\sigma}}^{\mathrm{x}}\right) \tag{18}$$

by means of the least-squares method. We have (see the appendix of [26])

$$\hat{\boldsymbol{\sigma}} = \left(\mathbb{X}^{\mathrm{T}}\,\mathbb{V}^{-1}_{\boldsymbol{\sigma}^{\mathrm{x}}_{\mathrm{exp}}}\,\mathbb{X}\right)^{-1}\mathbb{X}^{\mathrm{T}}\,\mathbb{V}^{-1}_{\boldsymbol{\sigma}^{\mathrm{x}}_{\mathrm{exp}}}\,\boldsymbol{\sigma}^{\mathrm{x}}_{\mathrm{exp}}, \tag{19}$$

where $\mathbb{V}_{\boldsymbol{\sigma}^{\mathrm{x}}_{\mathrm{exp}}}$ is the covariance matrix of the experimental data $\boldsymbol{\sigma}^{\mathrm{x}}_{\mathrm{exp}}$.

In the relationship between the x-ray yields and the ionization cross sections, equation (17), the matrix $\mathbb{X}$ embodies the atomic relaxation parameters, whose uncertainties must be propagated to the variances of $\hat{\boldsymbol{\sigma}}$. We will designate the set of relaxation parameters by $\mathbf{p}$, and individual values will be identified by p_i. Since the experimental x-ray yields and the adopted p_i are statistically independent, we can determine the total variance of the cross sections as the sum of the variances arising from these two uncertainty sources; in other words, we employ the well-known 'sum in quadrature' rule for independent contributions to the uncertainty budget. Calculating the variances due to the $\hat{\boldsymbol{\sigma}}^{\mathrm{x}}$ in the framework of the least-squares method we get

$$\mathbb{V}_{\hat{\boldsymbol{\sigma}}} = \left(\mathbb{X}^{\mathrm{T}}\,\mathbb{V}^{-1}_{\boldsymbol{\sigma}^{\mathrm{x}}_{\mathrm{exp}}}\,\mathbb{X}\right)^{-1} + \mathbb{D}\,\mathbb{V}_{\mathrm{par}}\,\mathbb{D}^{\mathrm{T}}, \tag{20}$$

where $V_{\mathrm{par}\,ij} = \mathrm{var}(p_i)\delta_{ij}$ with $\mathrm{var}(p_i)$ the variance of p_i, and the matrix elements of $\mathbb{D}$ are the partial derivatives of the fitted values of the cross sections with respect to the p_i, $D_{\nu i} = \partial\hat{\sigma}_\nu/\partial p_i$. These derivatives are computed numerically interpreting the components $\hat{\sigma}_\nu$ of expression (19) as functions of the p_i. The second term in the right-hand side of equation (20) corresponds to the usual approximate formula for variance propagation, conveniently written in matrix form (see e.g. section 2.4.5 of [27]). We point out that the covariances between the atomic relaxation parameters were set to zero because, to the best of our knowledge, they have never been evaluated.

For electron energies above $U_{\mathrm{Au\,K}}$, the migration of a K-shell vacancy to any L subshell must be considered. In these cases (89.88 and 100.43 keV runs), the K-shell ionization cross section $\hat{\sigma}_{\mathrm{K}}$ is added to the vector $\hat{\boldsymbol{\sigma}}$ of parameters to be fitted, and the column vector $\boldsymbol{\sigma}^{\mathrm{x}}_{\mathrm{exp}}$ is augmented with the measured Kα_1, Kα_2 and K$\beta_{1,3}$ x-ray production cross sections deduced from the corresponding peak areas. Thus, for $E > U_{\mathrm{Au\,K}}$ we can also estimate $\hat{\sigma}_{\mathrm{K}}$.

Ionization cross sections were calculated with two datasets of atomic relaxation parameters to assess the sensitivity of the methodology to these quantities. The classic dataset, C, contains fluorescence yields and Coster–Kronig coefficients compiled by Krause [28], radiative and nonradiative vacancy-transfer probabilities from K shell to the L_i subshells given by [29, 30], respectively, and x-ray emission rates taken from [29]. The emission rates from [29] have uncertainties of the order of 5% [31]. In turn, the most recent values were collected in dataset R, which consists in fluorescence yields and Coster–Kronig coefficients given by Kolbe *et al* [32], radiative and non-radiative vacancy-transfer probabilities from the K shell to L_i subshells calculated by Scofield [33] and Rao [30], respectively, and x-ray emission rates tabulated by Campbell and Wang [34]. The transfer probabilities from [33] have uncertainties of the order of 2% [31] and the fraction of the Auger contribution in η_{KL_i} introduces an uncertainty of about 15% [30]. Both datasets are summarized in tables 1 to 3.

4. Results

Table 4 summarizes our experimental Lα, Lβ, Lγ, Lℓ and Lη x-ray production cross sections deduced from equation (4), and figure 5 displays them together with experimental values reported by other authors [8, 9, 11, 35, 36]. Figure 5 also

Table 1. Fluorescence yields and Coster–Kronig transition probabilities. The uncertainty of f'_{13} was not disclosed by the authors; we chose the quoted values arbitrarily although they can be multiplied by 10 barely affecting the total uncertainty of the cross sections.

Set	ω_1	ω_2	ω_3	f_{12}	f_{13}	f_{23}	f'_{13}
C [28]	0.107(16)	0.334(17)	0.320(10)	0.14(2)	0.53(3)	0.122(18)	0.0028(3)
R [32]	0.117(4)	0.359(13)	0.310(11)	0.064(40)	0.524(75)	0.180(40)	0.0028(3)

Table 2. Vacancy-transfer probabilities from the K shell to L_i subshells. The uncertainties were evaluated by the appropriate uncertainty propagation.

Set	η_{KL_1}	η_{KL_2}	η_{KL_3}
C [29, 30]	0.0074(1)	0.295(21)	0.504(35)
R [30, 33]	0.0069(10)	0.2943(67)	0.5025(68)

Table 3. Ratios of L-subshell x-ray emission rates. The relative uncertainties of the values in sets C and R are 5% and 0.2%, respectively [31].

Ratios of emission rates	Set C [29]	Set R [34]
$\Gamma_{L_3M_5}/\Gamma_{L_3,tot}$	0.7070	0.6999
$\Gamma_{L_3M_4}/\Gamma_{L_3,tot}$	0.0802	0.0796
$\Gamma_{L_3M_1}/\Gamma_{L_3,tot}$	0.0396	0.0393
$\Gamma_{L_2M_1}/\Gamma_{L_2,tot}$	0.0216	0.0217
$\Gamma_{L_2M_4}/\Gamma_{L_2,tot}$	0.7976	0.7893
$\Gamma_{L_3N_5}/\Gamma_{L_3,tot}$	0.1320	0.1385
$\Gamma_{L_1M_3}/\Gamma_{L_1,tot}$	0.3849	0.3956
$\Gamma_{L_1M_2}/\Gamma_{L_1,tot}$	0.3339	0.3414
$\Gamma_{L_2N_4}/\Gamma_{L_2,tot}$	0.1575	0.1649
$\Gamma_{L_1N_2}/\Gamma_{L_1,tot}$	0.0844	0.0885
$\Gamma_{L_1N_3}/\Gamma_{L_1,tot}$	0.1050	0.1118

Table 4. Measured Lα, Lβ, Lγ, Lℓ and Lη x-ray production cross sections of Au by electron impact. The numbers between parentheses are the uncertainties (one standard deviation) in units of the least significant digit.

E (keV)	$\sigma^x_{L\alpha}$ (b)	$\sigma^x_{L\beta}$ (b)	$\sigma^x_{L\gamma}$ (b)	$\sigma^x_{L\ell}$ (b)	$\sigma^x_{L\eta}$ (b)
51.07(4)	187(24)	133(17)	18.7(24)	10.7(14)	2.1(4)
56.46(4)	178(23)	127(16)	18.0(23)	9.7(13)	1.8(4)
61.07(4)	183(23)	129(17)	18.0(23)	9.5(13)	2.4(7)
65.85(4)	190(24)	132(17)	18.9(24)	10.2(14)	2.7(8)
70.45(4)	177(23)	124(16)	17.7(23)	9.0(13)	1.9(7)
79.96(4)	155(20)	112(14)	15.7(20)	7.6(10)	1.6(4)
89.88(4)	150(19)	109(14)	15.1(19)	7.9(10)	1.6(4)
100.43(4)	147(19)	107(14)	15.5(20)	7.9(10)	2.0(4)

shows theoretical x-ray production cross sections evaluated using equations (7) to (16) with ionization cross sections calculated in the framework of the DWBA [3, 4] and the C and R sets of relaxation parameters.

Figure 6 compares the experimental ratios $\sigma^x_{L\ell}/\sigma^x_{L\alpha}$ and $\sigma^x_{L\gamma_2}/\sigma^x_{L\gamma_3}$ to the ratios of emission rates tabulated in [29, 34].

In table 5 we collect the present L_1, L_2 and L_3 subshell ionization cross sections for Au, and the respective uncertainties, evaluated with the atomic relaxation parameters of set R (see tables 1 to 3). Table 5 includes the K-shell ionization cross sections obtained in the runs with electron energies above $U_{Au\,K}$. Figure 7 compares the L-subshell ionization cross sections with the experimental data found in the literature [5–11] and the predictions of the DWBA [3, 4]. Finally, figure 8 depicts the K-shell ionization cross section resulting from our data analysis along with the existing measurements [7, 12, 37, 38] and the theoretical values computed within the DWBA.

The Au L_1, L_2 and L_3 subshell ionization cross sections evaluated with atomic relaxation parameters from dataset C (not shown) do not display variations larger than the calculated uncertainties. These differences are approximately 13% for L_1, 4% for L_2 and 6% for L_3, all within the error bars of the ionization cross sections.

5. Discussion

In the first subsection we review the existing articles on L-subshell ionization by electron impact on Au atoms at energies below 100 keV. All the authors deduced the x-ray production cross sections using equation (4), but differed on the method of measurement of N_e and d. We shall call 'direct measurement' those where N_e is obtained measuring the beam current and the sample mass thickness is determined from any independent experiment. The term 'relative method' will mean that the product $N_e\,d$ was deduced in the same experiment from the bremsstrahlung yield and its accepted theoretical differential cross section. In our experiment we used the relative method, and in addition estimated the mass thickness of the Au film from the bremsstrahlung differential cross sections and the charge collected in the Faraday cup.

The other two subsections are devoted to the present ionization cross sections, generated with our analysis method and looking to what they would be if the more customary methodology for transforming x-ray production to L-subshell ionization cross sections were applied.

5.1. Literature review

Green and Cosslett [5] and Salem and Moreland [6] measured σ_{L_2} and σ_{L_3} from the ionization threshold up to about 50 keV by the direct method having recourse to wavelength-

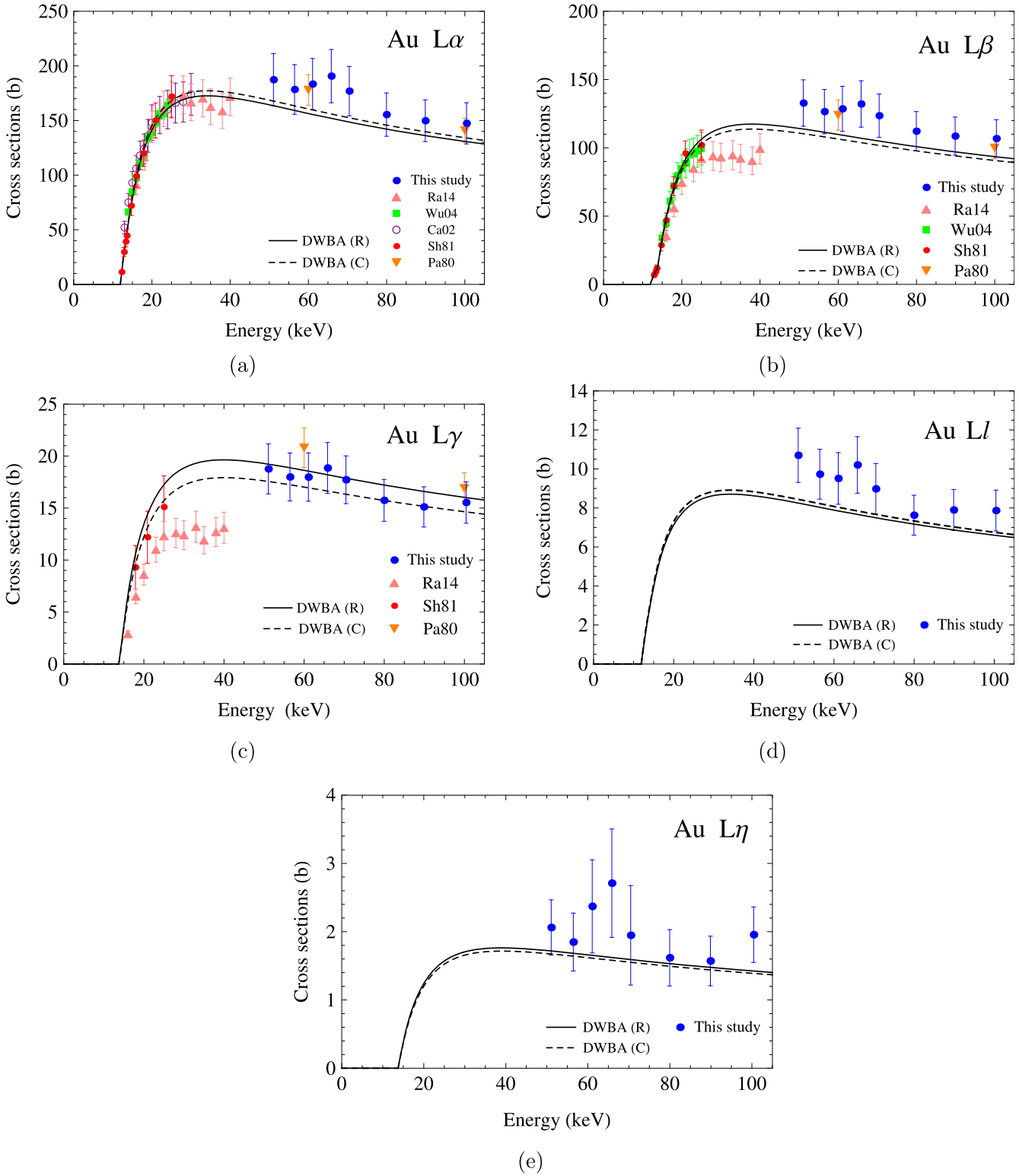

Figure 5. Au Lα, Lβ, Lγ, Lℓ and Lη x-ray production cross sections. The (blue) circles are our experimental values. (Green) squares, (purple) empty circles, (orange) inverted triangles, (red) circles and (pink) triangles represent the data from references Wu04 [35], Ca02 [36], Pa80 [8], Sh81 [9] and Ra14 [11], respectively. The dashed and continuous curves indicate the theoretical DWBA results [4] with atomic relaxation parameters from sets C and R, respectively.

dispersive spectrometers for the acquisition of x-ray spectra; all the other authors employed semiconductor detectors. Green and Cosllet used $\omega_2 = 0.51$ and $\omega_3 = 0.55$ for the fluorescence yields, while Salem and Moreland adopted $\omega_2 = 0.31$ and $\omega_3 = 0.27$ (datasets C and R became available some years after their works).

Davis *et al* [7] obtained σ_{L_3} using a Ge(Li) detector for electron energies between 20 and 140 keV by the direct

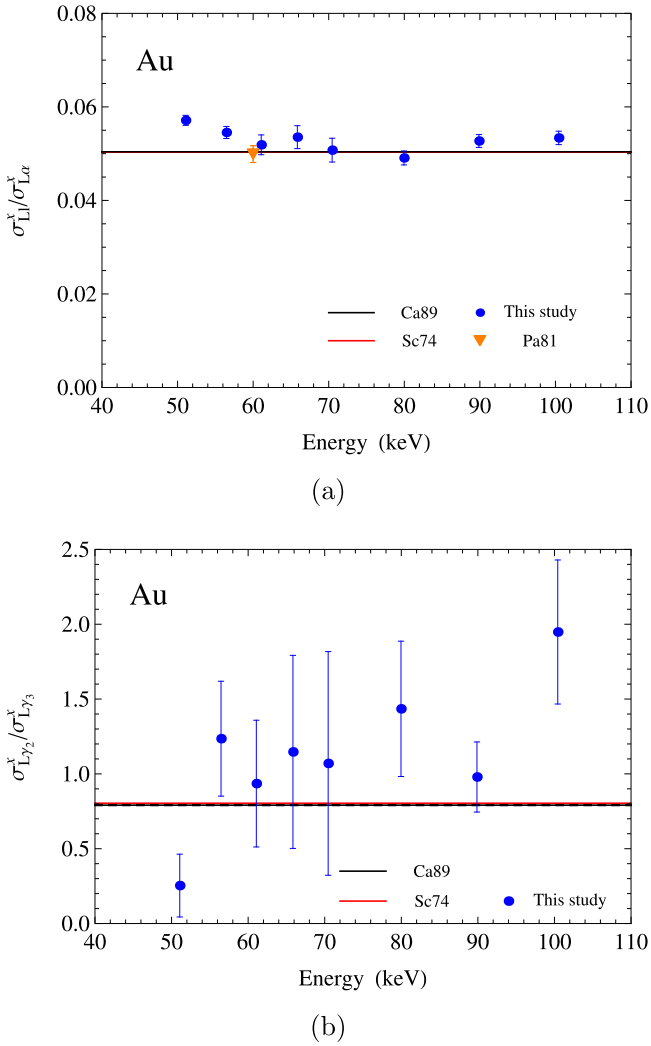

Figure 6. Experimental ratios (a) $\sigma^{x}_{L\ell}/\sigma^{x}_{L\alpha}$ and (b) $\sigma^{x}_{L\gamma_2}/\sigma^{x}_{L\gamma_3}$ for Au by electron impact. The horizontal lines, which can barely be distinguished, indicate the values tabulated by Campbell and Wang [34] (black continuous line) and Scofield [29] (red dashed line).

Table 5. L_1, L_2 and L_3 subshell and K-shell ionization cross sections for Au, evaluated with relaxation parameters from dataset R. The numbers between parentheses are the uncertainties (one standard deviation) in units of the least significant digit.

E (keV)	σ_{L_1} (b)	σ_{L_2} (b)	σ_{L_3} (b)	σ_K (b)
51.07(4)	149(38)	244(28)	697(75)	
56.46(4)	176(32)	218(26)	634(71)	
61.07(4)	188(45)	219(28)	631(76)	
65.85(4)	181(53)	235(30)	670(82)	
70.45(4)	173(60)	215(28)	605(78)	
79.96(4)	166(30)	187(23)	516(60)	
89.88(4)	146(22)	187(22)	523(59)	1.60(23)
100.43(4)	145(23)	190(22)	514(58)	2.90(38)

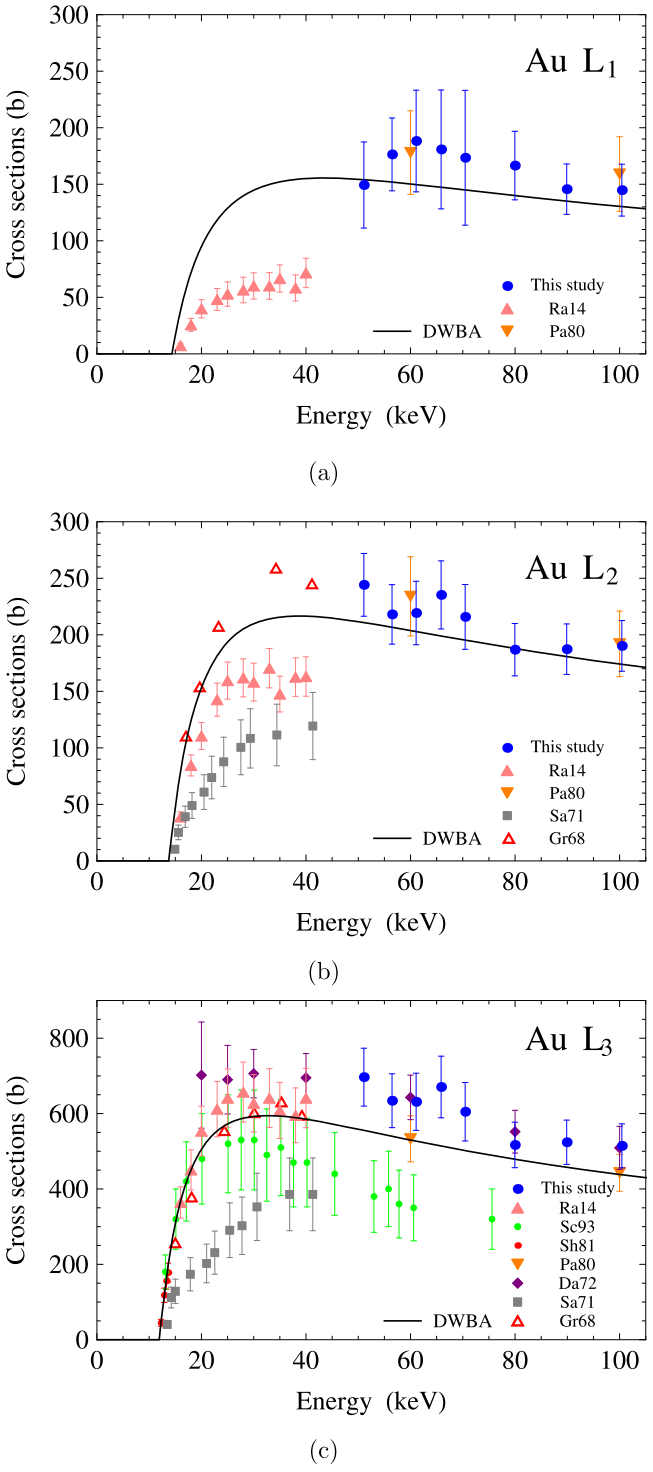

Figure 7. L_1, L_2 and L_3 subshell ionization cross sections of Au, evaluated with atomic relaxation parameters from set R. The (blue) circles are our experimental values. (Red) empty triangles, (grey) squares, (purple) diamonds, (orange) inverted triangles, (red) circles, (green) circles and (pink) triangles represent the data from references Gr68 [5], Sa71 [6], Da72 [7], Pa80 [8], Sh81 [9], Sc93 [10] and Ra14 [11], respectively. The continuous curves indicate the theoretical DWBA results [4].

method. For the fluorescence yields they took $\omega_3 = 0.32(3)$ but did not mention the adopted transition rates. Also, they did not explain how the continuous component of the spectrum was modelled in the evaluation of peak areas, despite the important efficiency jump at $U_{Ge\,K}$ in the spectra that leads to an uneven continuum under the Au L x-ray

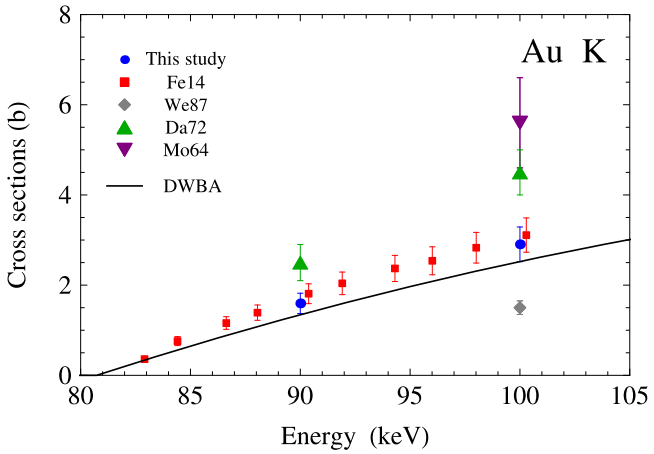

Figure 8. K-shell ionization cross section of Au. The (blue) circles are our experimental values at 89.88(4) and 100.43(4) keV. (Purple) inverted triangles, (green) triangles, (grey) diamonds and (red) squares represent the data from references Mo64 [37], Da72 [7], We87 [38] and Fe14 [12], respectively. The continuous curve is the prediction of the DWBA [4].

peaks. This difficulty may be the reason why all other works reviewed below acquired the x-ray spectra with Si(Li) spectrometers.

Shima *et al* [9] measured Au Lα, Lβ and Lγ x-ray production cross sections by the direct method from threshold to 25 keV, but extracted σ_{L_3} only up to 13.6 keV, i.e. below the L_2 threshold. Their sample consisted in a 7 μg cm^{-2} Au film deposited on a 4–8 μg cm^{-2} C substrate. The relaxation parameters were taken from [28, 39].

Schneider *et al* [10] determined σ_{L_3} with uncertainties of 25% at energies ranging from 12.3 to 75 keV by the relative method. They irradiated Au samples with thicknesses of 80–100 nm, sufficiently thick to scatter most of the electrons in the beam at the lower energies, although the authors did not take into account this effect when evaluating the bremsstrahlung cross section and the electron path length in the Au film. The fluorescence yields were taken from [28, 40] and they resorted to theoretical σ_{L_2} and σ_{L_1} values calculated within the plane-wave Born approximation with semi-empirical Coulomb and exchange corrections. The relative method was tested by Campos *et al* [36], who reported Lα x-ray production cross sections from 10 to 30 keV by the direct and relative methods, finding consistent results with relative uncertainties of 11%. However, they employed Au films with mass thicknesses around 14 μg cm^2 deposited on a thick C substrate, and corrected for the presence of the thick substrate resorting to Monte Carlo simulations. Campos *et al* adopted emission rates, fluorescence yields and Coster–Kronig transition probabilities from [40, 41].

Pálinkás and Schlenk [8] reported Au Lα, Lβ and Lγ x-ray production cross sections, measured by the direct method at electron energies ranging from 60 to 600 keV. The samples had mass thicknesses between 20 and 200 μg cm^{-2}, and they were either self-supporting or deposited over 2-μg cm^{-2}-thick C backings (the targets with mass thicknesses greater than 80 μg cm^{-2} were used only for energies above 300 keV). The values of σ_{L_1}, σ_{L_2} and σ_{L_3} were derived from the Lα, Lγ_1 and L$\gamma_{2,3,6}$ lines with the method denoted as TRY3 in Cohen's review [24], taking the atomic relaxation parameters from [28, 29].

Rahangdale *et al* [11] recently measured Au Lα, Lβ and Lγ x-ray production cross sections from 15 to 40 keV by the direct method, and deduced the L_1, L_2 and L_3 subshell ionization cross sections. Their Au films had mass thicknesses between 50 and 120 μg cm^{-2}, and were either self-supporting or deposited over a 20-μg cm^{-2}-thick C foil. The authors compared the results with two sets of atomic relaxation parameters, one from [34, 42] and the other from [28, 29], and found differences that reached about 30% for σ_{L_1}, while for σ_{L_2} and σ_{L_3} the differences were smaller, about 10%. This agrees qualitatively with our findings, but we got a smaller difference for σ_{L_1}, of 13%. The values of σ_{L_1}, σ_{L_2} and σ_{L_3} were estimated from the Lα and L$\gamma_{1,2,3,5}$ x-ray production cross sections (TRY3 method [24]).

None of the aforementioned references discusses the propagation of the uncertainties associated to the atomic relaxation parameters to the standard deviations of the estimated σ_{L_i} cross sections, despite that some of the parameters have large uncertainties. Most of the authors made use of the parameters of dataset C, which implies a lower bound of 10% for the uncertainty. As a consequence, quoted uncertainties for subshell ionization cross sections smaller than 10% were calculated without taking into account the uncertainties of the relaxation parameters and are hence underestimated.

5.2. Present ionization cross sections

Figure 5 shows that our Lα and Lβ x-ray production cross sections are less than 20% higher than the calculations based on the DWBA, and they are consistent for the Lγ group. Our Lα, Lβ and Lγ x-ray emission cross sections are higher than those measured by Wu *et al* [35] and Shima *et al* [9], and agree with Campos *et al* [36] and Pálinkás and Schlenk [8]. Figure 6 shows that the ratios $\sigma^{x}_{L\ell}/\sigma^{x}_{L\alpha}$ and $\sigma^{x}_{L\gamma_2}/\sigma^{x}_{L\gamma_3}$ are practically constant within error bars for all irradiation energies and mostly compatible with the $\Gamma_{L_3M_1}/\Gamma_{L_3M_{4,5}}$ and $\Gamma_{L_1N_2}/\Gamma_{L_1N_3}$ values from Scofield [29] and Campbell and Wang [34].

The present σ_{L_1} and σ_{L_2} cross sections are consistent with the *ab initio* DWBA calculations, while the σ_{L_3} cross sections are about 20% above this model. When compared with existing data from the literature (see figure 7) we find that our measurements agree with the values of Pálinkás and Schlenk [8] for the three L subshells and with those of Green and Cosslett [5] for σ_{L_2} and σ_{L_3}. Our results for σ_{L_3} are also in accord with the measurements of Davis *et al* [7] and Rahangdale *et al* [11]. However, our experimental cross sections are substantially above those published by Rahangdale *et al* [11] for L_1 and L_2, Salem and Moreland [6] for L_2, and Schneider *et al* [10] for L_3. The present K-shell ionization cross sections (figure 8) match with the very recent measurements by our group [12] and are close to the predictions of the DWBA.

The L_1 subshell ionization cross sections have uncertainties that are two to three times larger than those of the other subshells. This happens because σ_{L_1} depends on the $L\beta_3$, $L\beta_4$, $L\gamma_2$ and $L\gamma_3$ x-ray production cross sections, which were estimated with lower accuracies and therefore had high uncertainties; the atomic parameters also contribute to the increased uncertainties because ω_1 has a standard deviation which is about three times that of ω_2 and ω_3.

The relative uncertainties in the Au L_1, L_2 and L_3 subshell ionization cross sections would be approximately 22, 11 and 12%, respectively, if the uncertainties of the atomic relaxation parameters involved in the fit were ignored. When equation (20) is used to propagate the uncertainties of these parameters, with dataset R we get uncertainties of 23, 12 and 13%, respectively, which increase to 28, 16 and 16%, respectively, if dataset C is adopted. There is a lower bound to the uncertainties of the subshell ionization cross sections, which is directly related to the uncertainties of the relaxation parameters. This value is 10% for dataset C and 5% for dataset R. Accordingly, more accurate relaxation parameter values, particularly fluorescence yields and transition rates, are necessary to measure these cross sections with smaller uncertainties.

The application of equation (4) assumes an isotropic angular distribution of the emitted characteristics x-rays. It is well known that ionization by electrons, high-velocity ions and photons [43] leads to the alignment of inner-shell vacancies with total angular momentum $j > \frac{1}{2}$ because the magnetic sublevels of the ionized atom have a nonstatistical population. Thus, we do expect isotropic emission only for the lines of multiplet $L\gamma$, which come from vacancies in the subshells L_1 and L_2. The lines $L\alpha_1$ and $L\alpha_2$ of the $L\alpha$ doublet, $L\beta_{2,15}$ and $L\beta_6$ of the $L\beta$ multiplet and the $L\ell$ line originate from vacancies in the L_3 subshell, which has $j = \frac{3}{2}$; hence, these lines ought to present some degree of anisotropy. The $L\beta_{2,15}$ and $L\beta_6$ lines are low-intensity components and therefore the effect of anisotropy on the $L\beta$ multiplet as a whole should be small, but the anisotropy of the $L\alpha$ and $L\ell$ lines could be non-negligible. Most studies consider nevertheless an isotropic angular distribution for all the L lines generated by electron impact [8, 9, 11, 35, 36], as we did here. Anyway, this topic deserves further investigation because the experimental studies are inconclusive: some authors observe an anisotropic angular distribution for $L\alpha$ [44] while others do not find any angular dependence for the intensity of this doublet [45].

Although we recorded the x-ray spectra with a HPGe detector, the procedure used to fit the peak areas of the $L\ell$ and $L\eta$ lines enabled their unfolding with good precision. The same happened with lines $L\gamma_1$, $L\gamma_2$ and $L\gamma_3$ of the $L\gamma$ group (see figure 6). It was not possible to unfold the lines of the $L\alpha$ and $L\beta$ peaks. In this respect, Si(Li) or Si drift x-ray detectors are preferable due to their better energy resolution and because their FE peak efficiency curves do not have a discontinuity in the L group x-rays region. These features facilitate the unfolding of the $L\beta$ group.

5.3. Ionization cross sections derived from our x-ray production cross sections applying other analysis methods

For the sake of completeness we have also evaluated the L-subshell ionization cross sections in two other ways that are applied in most of the cited references, namely using either $L\alpha$, $L\beta$ and $L\gamma$ (TRY1 [24]) or $L\alpha$, $L\gamma_1$ and $L\gamma_{2,3}$ (TRY3 [24]) x-ray production cross sections. TRY1 leads to large uncertainties for σ_{L_1} and sometimes even negative values as mentioned by Pálinkás and Schlenk [8], Cohen [24] and Miranda and Lapicki [2]. The TRY3 method (employed in [8, 11]) yielded ionization cross sections close to those of table 5 although with slightly larger uncertainties, partly because some of the measured x-ray production cross sections are dismissed.

6. Conclusions

We have measured the Au $L\alpha$, $L\beta$, $L\gamma$, $L\ell$ and $L\eta$ x-ray production cross sections and the L_1, L_2 and L_3 ionization cross sections by electron impact for kinetic energies from 50 to 100 keV. The experimental values are compared with the *ab initio* DWBA calculations and measurements found in the literature. Our experimental L_1 and L_2 subshell ionization cross sections are consistent with the DWBA, and the results for the L_3 subshell are slightly above this formalism although the measured σ_{L_3} is generally in agreement with the most recent data published by other authors. On the other hand, significant discrepancies are observed between the available experimental σ_{L_2} and σ_{L_1} cross sections. Therefore, it is premature to draw definitive conclusions either on the theoretical side or on the adopted atomic parameter values.

The developed least-squares procedure worked well, yielding uncertainties that take into account the standard deviations of the fundamental atomic parameters and a quantitative test of the quality of the fit, through the chi-square test. The atomic relaxation data uncertainties must be estimated with better accuracy to reduce the error bars in the measured ionization cross sections, since they impose a lower bound in the uncertainties of the atomic ionization cross sections. Gathering experimental intensities for more L x-ray components with higher counting statistics can shed light into some of the atomic relaxation parameters because more lines will provide information for each subshell cross section. Inconsistencies in the fluorescence yields and Coster–Kronig coefficients will increase chi-square to the rejection zone, independent of the cross-section values. It may be possible to fit a few of these coefficients, since there will be more degrees of freedom in the system of equations.

Acknowledgments

We thank MSc W G P Engel for preparing the sample, and Professor M N Martins and the technical staff of the São Paulo Microtron for their valuable help in the operation of the

accelerator. We are also indebted to Dr X Llovet for clarifying discussions. This work was performed with funding from the Brazilian agencies FAPESP (Fundação de Amparo à Pesquisa do Estado de São Paulo) and CNPq (Conselho Nacional de Desenvolvimento Científico e Tecnológico). J M Fernández-Varea thanks the financial support from the Brazilian Coordenação de Aperfeiçoamento de Pessoal de Nível Superior (program CAPES-PVE) as well as the Generalitat de Catalunya (project no. 2014 SGR 846).

References

[1] Llovet X, Powell C J, Salvat F and Jablonski A 2014 *J. Phys. Chem. Ref. Data* **43** 013102
[2] Miranda J and Lapicki G 2014 *At. Data Nucl. Data Tables* **100** 651
[3] Bote D and Salvat F 2008 *Phys. Rev. A* **77** 042701
[4] Llovet X, Salvat F, Bote D, Salvat-Pujol F, Jablonski A and Powell C J 2014 *NIST Database of Cross sections for Inner-Shell Ionization by Electron or Positron Impact, Version 1.0* (NIST Standard Reference Database) 164 http://dx.doi.org/10.6028/NIST.NSRDS.164
[5] Green M and Cosslett V E 1968 *J. Phys. D* **1** 425
[6] Salem S I and Moreland L D 1971 *Phys. Lett* **37A** 161
[7] Davis D V, Mistry V D and Quarles C A 1972 *Phys. Lett* **38A** 169
[8] Pálinkás J and Schlenk B 1980 *Z. Phys.* A **197** 29
[9] Shima K, Nakagawa T, Umetani K and Mikumo T 1981 *Phys. Rev.* A **24** 72
[10] Schneider H, Tobehn I, Ebel F and Hippler R 1993 *Phys. Rev. Lett.* **71** 2707
[11] Rahangdale H V, Guerra M, Das P K, De S, Santos J P, Mitra D and Saha S 2014 *Phys. Rev. A* **89** 052708
[12] Fernández-Varea J M, Jahnke V, Maidana N L, Malafronte A A and Vanin V R 2014 *J. Phys. B: At. Mol. Opt. Phys* **47** 155201
[13] Vanin V R, Manso Guevara M V, Maidana N L, Martins M N and Fernández-Varea J M 2015 *Radiat. Phys. Chem.* submitted
[14] Seltzer S M and Berger M J 1986 *At. Data Nucl. Data Tables* **35** 345
[15] Pratt R H, Tseng H K, Lee C M and Kissel L 1977 *At. Data Nucl. Data Tables* **20** 175
Pratt R H, Tseng H K, Lee C M and Kissel L 1981 *At. Data Nucl. Data Tables* **26** 477 (erratum)
[16] Kissel L, Quarles C A and Pratt R H 1983 *At. Data Nucl. Data Tables* **28** 381
[17] Maidana N L, Vanin V R, Jahnke V, Fernández-Varea J M, Martins M N and Brualla L 2013 *Nucl. Instrum. Methods* A **729** 371
[18] Seltzer S M 1981 *Nucl. Instrum. Methods* **188** 133
[19] Gao F, Campbell L W, Devanathan R, Xie Y L, Zhang Y, Peurrung A J and Weber W J 2007 *Nucl. Instrum. Methods* B **255** 286
[20] Deslattes R D, Kessler E G Jr, Indelicato P, Billy L, Lindroth E and Anton J 2003 *Rev. Mod. Phys* **75** 35
[21] Wegrzynek D, Markowicz A and Cuevas A M 2001 *X-Ray Spectrom.* **30** 403
[22] Dingfelder M, Segui S and Fernández-Varea J M 2008 *Phys. Rev.* A **77** 062710
[23] Fernández-Varea J M, Segui S and Dingfelder M 2011 *Phys. Rev.* A **83** 022702
[24] Cohen D D 1984 *J. Phys. B: At. Mol. Phys.* **17** 3913
[25] Reusch S, Genz H, Löw W and Richter A 1986 *Z. Phys.* D **3** 379
[26] Helene O and Vanin V R 1993 *Nucl. Instrum. Methods* A **335** 227
[27] Eadie W T, Drijard D, James F E, Roos M and Sadoulet B 1971 *Statistical Methods in Experimental Physics* (Amsterdam: North Holland)
[28] Krause M O 1979 *J. Phys. Chem. Ref. Data* **8** 307
[29] Scofield J H 1974 *At. Data Nucl. Data Tables* **14** 121
[30] Rao P V 1972 *Phys. Rev.* A **5** 997
[31] Madison D H and Merzbacher E 1975 *in Atomic Inner-Shell Processes* ed B Crasemann (New York: Academic Press) pp 1–69
[32] Kolbe M, Hönicke P, Müller M and Beckhoff B 2012 *Phys. Rev.* A **86** 042512
[33] Scofield J H 1974 *Phys. Rev.* A **9** 1041
[34] Campbell J L and Wang J X 1989 *At. Data Nucl. Data Tables* **43** 281
[35] Wu Y, An Z, Liu M T, Duan Y M, Tang C H and Luo Z M 2004 *J. Phys. B: At. Mol. Opt. Phys.* **37** 4527
[36] Campos C S, Vasconcelos M A Z, Llovet X and Salvat F 2002 *Phys. Rev.* A **66** 012719
[37] Motz J W and Placious R C 1964 *Phys. Rev.* **136** A662
[38] Westbrook G L and Quarles C A 1987 *Nucl. Instrum. Methods* B **24/25** 196
[39] Scofield J H 1974 *Phys. Rev.* A **10** 1507
[40] Werner U and Jitschin W 1988 *Phys. Rev.* A **38** 4009
[41] Scofield J H 1969 *Phys. Rev.* **179** 11
[42] Campbell J L 2003 *At. Data Nucl. Data Tables* **85** 291
[43] Berezhko E G and Kabachnik N M 1977 *J. Phys. B: At: Mol. Phys.* **10** 2467
[44] Wang X, Xu Z, Zhang L, Hu P and Shi X 2014 *Radiat. Phys. Chem.* **103** 213
[45] Sestric G, Ferguson S, Wright I and Williams S 2014 *Radiat. Phys. Chem.* **102** 40